

Target-Conformal Optimization-Based Actuator Placement for Ultrasound-Mediated Hyperthermia in Cancer Treatments

D. A. Deenen^{ID}, L. C. Sebeke, B. de Jager^{ID}, E. Heijman^{ID}, H. Gröll,
and W. P. M. H. Heemels^{ID}, *Fellow, IEEE*

Abstract—In hyperthermia for cancer treatments, tumors are heated to improve the outcome of radio- and chemotherapies. Using extracorporeal high-intensity focused ultrasound (HIFU) transducers, the heating can be applied noninvasively, accurately, and with high acoustic power. The heating location can be changed by electronic beam steering, within the transducer’s small local heating range, and by mechanically repositioning the transducer, which effectively shifts the local range to enable the treatment of larger tumors. An important problem is the selection of the sonication points, i.e., the discrete locations reachable by electronic beam steering, and the admissible mechanical transducer positions, which must be performed prior to treatment, and can be seen as an actuator selection problem. Clearly, the selected sonication points and transducer positions have a major impact on the achievable tumor temperatures, and their number is directly related to the controller’s complexity and, thereby, real-time feasibility. To address this challenging problem, this brief presents a target-conformal optimization-based actuator placement procedure, designed to assist the clinician in enabling maximum treatment quality using only a limited number of sonication points and transducer positions. The method is computationally tractable, and takes into account the specific tumor geometry and tissue properties.

Index Terms—Hyperthermia, input selection, model predictive control (MPC), oncology, optimization.

I. INTRODUCTION

IT HAS been shown in many clinical trials that heating tissues to approximately 42 °C over an extended period of time, referred to as mild hyperthermia, significantly enhances the desired effects of chemo- and radiotherapy [1], [2]. Using radio frequency waves or high-intensity focused ultrasound (HIFU) as heating modality, hyperthermic temperatures can be

induced in tissue. In recent years, HIFU has been successfully combined with near-real-time temperature measurements obtained using an MRI scanner, resulting in magnetic-resonance-guided (MR-)HIFU as a valuable technology for feedback-controlled thermal therapies [3]. Modern MR-HIFU setups typically use phased-array transducers, which enable powerful heating with millimeter-scale accuracy, allowing for high-quality treatments. In particular, a focal spot can be generated by constructive interference of the ultrasound waves and steered up to a (typically small) maximum deflection via coordinated phase shifts of the acoustic driving signals, which is referred to as electronic beam steering. Consequently, HIFU allows for much higher spatial heating accuracy than achievable using RF phased-array transducers, but was typically only suitable for the treatment of small tumors. For high-accuracy HIFU hyperthermia treatments of large tumors, the HIFU transducer itself can be repositioned mechanically [4], [5].

The discrete locations to which the focal spot can be steered during treatment are called sonication points. Together with the admissible transducer positions, these must be chosen by the clinician during pretreatment planning [6], such that subsequently a feedback controller can be used to determine the desired transducer position and sonication point powers during treatment. However, choosing the sonication points and admissible transducer positions that enable optimal treatment temperatures is: 1) not straightforward, as this strongly depends on the specific tumor shape and tissue properties but; 2) of vital importance, as the therapeutic effects of hyperthermia are directly linked to the realized tumor temperatures [7]. Moreover, including more points and positions generally allows for better control performance, but also increases controller complexity, which is especially for more advanced (and thereby computationally demanding) strategies such as model predictive control (MPC) [8], [9], [10], [11], [12], [13], [14] may hamper real-time feasibility. Hence, an important problem is the selection of a sufficiently small set of sonication points and transducer positions that balances the control ability and computational feasibility of the online control scheme.

In line with the above, as the first and main contribution of this brief, we propose a target-conformal optimization-based actuator placement method for MR-HIFU hyperthermia treatments, which enables the clinician to maximize treatment quality using only a limited number of sonication points and transducer positions, while taking into account the specific

Manuscript received 27 September 2022; accepted 19 January 2023. This work was supported in part by the Dutch Cancer Society and the Netherlands Organisation for Scientific Research (NWO) as part of their joint Partnership Programme: “Technology for Oncology,” in part by the Top Sector Life Sciences and Health “PPP Allowance,” in part by the European Union “IPaCT,” and in part by the German Federal Ministry of Education and Research “MR-HIFU-Pancreas.” Recommended by Associate Editor M. Grover. (*Corresponding author: D. A. Deenen.*)

D. A. Deenen, B. de Jager, and W. P. M. H. Heemels are with the Department of Mechanical Engineering, Eindhoven University of Technology, 5600 MB Eindhoven, The Netherlands (e-mail: d.a.deenen@tue.nl; a.g.de.jager@tue.nl; m.heemels@tue.nl).

L. C. Sebeke and H. Gröll are with the Department of Diagnostic and Interventional Radiology, University Hospital of Cologne, 50937 Cologne, Germany (e-mail: lukas.sebeke@uk-koeln.de; holger.gruell@uk-koeln.de).

E. Heijman is with Philips Research, 5656 AE Eindhoven, The Netherlands (e-mail: edwin.heijman@philips.com).

Color versions of one or more figures in this article are available at <https://doi.org/10.1109/TCST.2023.3245336>.

Digital Object Identifier 10.1109/TCST.2023.3245336

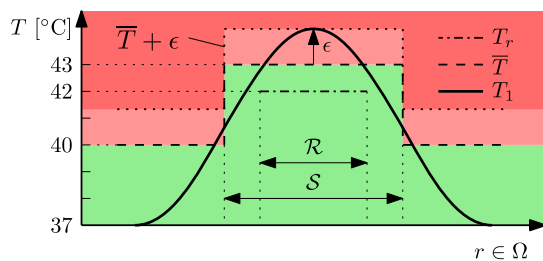


Fig. 1. Schematic cross section of the temperature objectives corresponding to \mathcal{R} and \mathcal{S} . The maximum violation ϵ is shown for some overheated temperature distribution T_1 such that $T_1 \leq \bar{T} + \epsilon$.

tumor geometry and tissue properties. As a second contribution, the resulting control performance and computation times are investigated for various actuator settings in a large-volume (requiring multiple admissible transducer positions) MR-HIFU hyperthermia numerical case study using MPC, as this is among the most promising control solutions for high-precision thermal therapies, but is also prone to high computational burden [8], [9], [10], [11], [12], [13], [14].

II. HYPERTHERMIA TREATMENT AND SETUP

A. Hyperthermia Treatment

During pretreatment planning, the clinician typically defines the target area and the critical structures that should be protected [6]. The temperature objectives for hyperthermia therapy are schematically depicted in cross section perspective in Fig. 1 for a target region of interest (ROI) \mathcal{R} , which includes the tumor, and a safety boundary region \mathcal{S} in the patient domain Ω , where $\mathcal{R} \subset \mathcal{S} \subset \Omega$. The main goal is to achieve constant and uniform heating of \mathcal{R} , with optimal treatment quality being achieved at 42 °C [15], [16], indicated by the reference temperature $T_r : \mathcal{R} \rightarrow \mathbb{R}$ in the figure. However, temperatures above 43 °C inside the ROI must be prevented, as this significantly deteriorates treatment quality and may cause direct tissue damage. In addition, the tissue outside \mathcal{S} must remain cooler than 40 °C, to avoid sensitization of the healthy tissue. Correspondingly, the temperature upper bound $\bar{T} : \Omega \rightarrow \mathbb{R}$ is defined. The maximum violation of this bound is indicated by $\epsilon \in \mathbb{R}_{\geq 0}$, as will be explained in more detail below.

B. MR-HIFU Hyperthermia System

In this work, we consider an MR-HIFU hyperthermia treatment setup consisting of a Philips 3T Achieva MRI scanner, with which volumetric temperature maps can be obtained noninvasively and in near-real time, and a Profound Sonalleve HIFU applicator platform, schematically depicted in Fig. 2, consisting of a patient bed in which an MR-compatible HIFU transducer and its mechanical robotic carrier are integrated.

1) *MR Thermometry*: In this work, we use an MR thermometry grid consisting of $2.25 \times 2.25 \text{ mm}^2$ voxels (grid lines in Fig. 3) with MR sample time $T_s = 3.2 \text{ s}$. The set of $n_x \in \mathbb{N}_{>0}$ voxel center coordinates is denoted by $\mathcal{V} = \{r_v^1, \dots, r_v^{n_x}\}$, where $r_v^i \in \Omega$ for $i \in \mathbb{N}_{[1, n_x]}$.

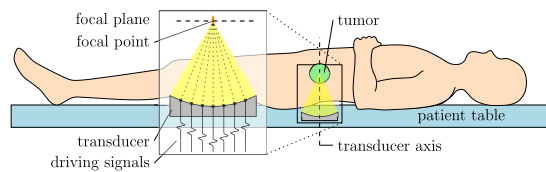


Fig. 2. Schematic of a HIFU beam into the focal plane in the tumor, with the focal point by electronic beam steering.

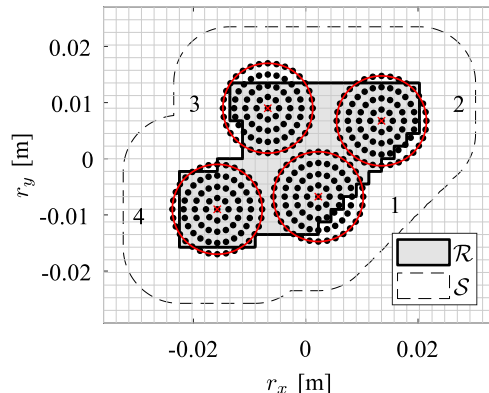


Fig. 3. Large irregular ROI \mathcal{R} with safety boundary region \mathcal{S} , four transducer positions \mathcal{T} (red \times) with their treatment cells (red circles), sonication points \mathcal{P} (\bullet) inside the treatment cells $\mathcal{C}(\mathcal{T})$, and the voxel grid \mathcal{V} (grid lines) which corresponds to the MR thermometry's spatial resolution.

2) *HIFU Transducer*: By constructively interfering ultrasound waves generated by the 256 acoustic elements of the phased-array HIFU transducer inside the Sonalleve system, a focal spot can be created, see Fig. 2. Using coordinated phase shifts in the driving signals, the focus location can be moved, which is called electronic beam steering, up to a lateral deflection of $R_{\text{EBS}} = 8 \text{ mm}$. The focus is relatively long along the beam axis (7 mm), but narrow in the lateral direction (2 mm), and additionally, significant acoustic beam overlap occurs directly in front of and behind the focal plane. Consequently, the temperature distribution inside the focal plane often characterizes the temperature in its surrounding volume, and can therefore be used as a reference for 3-D feedback control during treatment [5], [12], [13], [17]. Correspondingly, we choose the focal plane such that it bisects the target volume, and consider only the patient domain in this plane, i.e., $\Omega \subset \mathbb{R}^2$, in designing the temperature controller. However, note that the actuator placement procedure shown in this work can also be applied in 3-D.

The transducer itself can be mechanically relocated using the robotic arm on which it is mounted [5]. For a given transducer position, we call the 16 mm diameter ($=2R_{\text{EBS}}$) circular area in the patient domain Ω around the transducer axis, corresponding to the maximum electronic beam steering range, a treatment cell. For larger tumors, multiple transducer positions and their corresponding (possibly overlapping) treatment cells must be defined. We denote the set of $N_q \in \mathbb{N}_{>0}$ transducer axis positions by $\mathcal{T} = \{r_t^1, \dots, r_t^{N_q}\}$, with $r_t^q \in \Omega$ for $q \in \mathcal{Q} = \mathbb{N}_{[1, N_q]}$. The union of the resulting treatment cells, which effectively describes the area to which direct heating can potentially be applied, is then given by $\mathcal{C}(\mathcal{T}) = \bigcup_{q \in \mathcal{Q}} \mathcal{D}(r_t^q, R_{\text{EBS}})$, where $\mathcal{D}(r_t, R_{\text{EBS}}) = \{r \in \mathbb{R}^2 \mid$

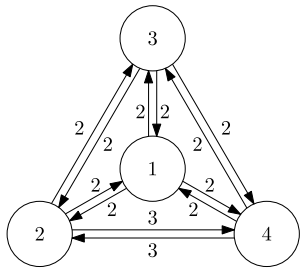


Fig. 4. Example of arc-weighted digraph with $N_q = 4$ for modeling the mechanical transducer motion.

$\{\|r - r_t\|_2 \leq R_{\text{EBS}}\}$ denotes the disk centered at r_t with radius equal to the electronic beam steering range R_{EBS} . An example is shown in Fig. 3, depicting a target ROI \mathcal{R} , a safety region \mathcal{S} , and four transducer positions \mathcal{T} (red \times) with corresponding treatment cells $\mathcal{C}(\mathcal{T})$ (red circles).

The discrete points to which the focus can be steered during treatment, and for which the desired heating powers can be determined by feedback control, are called *sonication points*. We denote the set of $n_u \in \mathbb{N}_{>0}$ sonication points as $\mathcal{P} = \{r_p^1, \dots, r_p^{n_u}\}$, where $r_p^i \in \Omega$ for $i \in \mathbb{N}_{[1, n_u]}$. Note that the sonication points must be chosen inside the treatment cells, i.e., $\mathcal{P} \subset \mathcal{C}(\mathcal{T})$, since they are otherwise not reachable (via electronic beam steering) using the transducer positions \mathcal{T} . In Fig. 3, an example for \mathcal{P} is shown (\bullet).

For a given transducer position, the focus can be quickly switched via electronic beam steering between all sonication points inside the corresponding treatment cell to achieve temporally quasi-continuous heating within the cell. The different cells can be heated sequentially by mechanically switching between the transducer positions [5]. It is the *objective* of this work to provide a method for selecting a limited number of transducer positions \mathcal{T} and sonication points $\mathcal{P} \subset \mathcal{C}(\mathcal{T})$ that enable the synthesis of a real-time feasible feedback controller with which the objectives described in Section II-A can be optimally satisfied during treatment. The method takes into account the ROI \mathcal{R} and the tissue's thermal dynamics in response to heating.

III. THERMAL MODEL

A. Mechanical Transducer Motion

We first model the mechanical transducer positioning according to the SAcSS framework of [18] using an arc-weighted digraph $\Gamma = (\mathcal{Q}, \mathcal{E}, s)$, an example of which is depicted in Fig. 4 for $N_q = 4$ admissible transducer positions. Here, $\mathcal{Q} = \mathbb{N}_{[1, N_q]}$ (nodes) represents the set of N_q operational actuator modes, corresponding to the transducer being in each of its N_q admissible positions \mathcal{T} (which are to be determined during the upcoming actuator placement procedure). The weighted arcs $\mathcal{E} = \mathcal{Q}^2 \setminus \{(q, q) \in \mathcal{Q}^2\}$ (numbered arrows) correspond to all possible transducer position switches, where the arc weights $s_{q\tilde{q}} \in \mathbb{N}$, $(q, \tilde{q}) \in \mathcal{E}$, represent the setup times, i.e., the number of MR thermometry sampling periods required to mechanically move the transducer from position q to \tilde{q} (rounded upward). The setup times may depend on the distance and direction of motion between the transducer

positions, and hence are generally a function of \mathcal{T} . Next, the actuator state is denoted by $\sigma_k \in \mathcal{Q} \cup \mathcal{E}$, where $\sigma_k = q \in \mathcal{Q}$ means that at discrete time $k \in \mathbb{N}$, connected to real time via $t_k = kT_s$, the transducer is in its q th admissible position, and $\sigma_k = (q, \tilde{q}) \in \mathcal{E}$ indicates that the transducer is being relocated from position q to \tilde{q} , during which no heating or measurement is possible.

B. Thermal Dynamics

Continuing the SAcSS framework [18], we model the tissue's thermal response using the discrete-time system

$$x_{k+1} = Ax_k + B(\mathcal{P})u_k \quad (1)$$

which is derived from the Pennes bioheat equation (PBHE) [19] with the homogeneous tissue parameters from [20]. Note that, typically, adequate model identification is required to obtain more accurate values for the tissue parameters, e.g., from previous treatment data or via low-power test shots [12]. The PBHE is spatially and temporally discretized using the MR thermometry grid, consisting of 2.25×2.25 mm² voxels with center points \mathcal{V} (see Section II-B1 and grid lines in Fig. 3), and the MR sample time $T_s = 3.2$ s mentioned previously. Consequently, $x_k \in \mathbb{R}^{n_x}$ represents the voxels' treatment-induced temperature elevation, where typically $n_x = 36^2 = 1296$ for tumors up to 4×4 cm², at discrete time $k \in \mathbb{N}$. Correspondingly, the matrix A has the form of a graph Laplacian matrix, capturing the effects of heat conduction inside the focal plane, and the heat loss resulting from blood perfusion. The input vector $u_k = [(u_k^1)^\top, \dots, (u_k^{N_q})^\top]^\top \in \mathbb{R}_{[0, u_{\max}}^{n_u}$ represents the acoustic powers applied at the sonication points $\mathcal{P} = \{r_p^1, \dots, r_p^{n_u}\}$, where the points $r_p^i \in \Omega$ are assumed to be ordered per treatment cell, such that $u_k^q \in \mathbb{R}^{n_u^q}$ denotes the powers of the n_u^q sonication points corresponding to cell $q \in \mathcal{Q}$, see also [18]. Note that $\sum_{q \in \mathcal{Q}} n_u^q = n_u$. Moreover, the lower input bound reflects that we cannot actively cool tissue, and the upper bound $u_{\max} = 15$ W is enforced for safety. In addition, the total input power is upper bounded by $\|u_k\|_1 \leq \bar{u}_\Sigma = 100$ W. To incorporate that heating can only occur at the sonication points of cell q if the transducer is at standstill in the corresponding position r_t^q , as indicated by $\sigma_k = q$, we impose $u_k^{\tilde{q}} = 0_{n_{\tilde{q}}}$ for all $\tilde{q} \in \mathcal{Q} \setminus \{\sigma_k\}$, where 0_n denotes the zero-vector of length n . Finally, the input matrix as a function of the sonication points $\mathcal{P} = \{r_p^1, \dots, r_p^{n_u}\}$ reads

$$B(\mathcal{P}) = [b(r_p^1) \quad \dots \quad b(r_p^{n_u})] \in \mathbb{R}^{n_x \times n_u} \quad (2)$$

where $b(r_p^i) \in \mathbb{R}^{n_x}$, $i \in \mathbb{N}_{[1, n_u]}$, describes the system's temperature change in response to unit heating at sonication point r_p^i , i.e., the j th element of $b(r_p^i)$ is given by $b_j(r_p^i) = T_s F(r_p^i, r_v^j)$, with acoustic deposition intensity $F(r_p^i, r_v^j) = \alpha_f \exp(-(\|r_v^j - r_p^i\|^2)/(2\sigma_f^2))$, where $\sigma_f = 2.4$ mm and $\alpha_f = 0.0267$, and T_s resulting from the Euler method.

IV. PROBLEM FORMULATION

The transducer positions \mathcal{T} and sonication points \mathcal{P} must be chosen before treatment to allow for controller synthesis.

Choosing them optimally is crucial for achieving desirable temperatures in (1), as via $B(\mathcal{P})$ this strongly depends on the points \mathcal{P} , which in turn are constrained by \mathcal{T} due to the finite electronic beam steering range requiring $\mathcal{P} \subset \mathcal{C}(\mathcal{T})$. Corresponding to the temperature objectives discussed in Section II-A and the spatial discretization of (1), optimizing the treatment quality can be expressed as minimizing the cost

$$\ell(z_k, \epsilon(x_k)) = (z_k - z_r)^\top Q(z_k - z_r) + f_\epsilon \epsilon(x_k) \quad (3)$$

where $z_k = Hx_k \in \mathbb{R}^{n_z}$, $n_z < n_x$, represents the target voxel temperatures, using the matrix $H \in \{0, 1\}^{n_z \times n_x}$ containing a single 1 per row and at most one 1 per column, and $z_r \in \mathbb{R}^{n_z}$ is the reference temperature corresponding to T_r on the voxel grid \mathcal{V} (see Section II). Similarly, $\epsilon(x_k) = \|\max\{x_k - \bar{x}, 0_{n_x}\}\|_\infty \in \mathbb{R}_{\geq 0}$, where the maximum operator is used element-wise, corresponds to the maximum violation of the temperature upper bound $\bar{x} \in \mathbb{R}^{n_x}$ obtained by spatially discretizing \bar{T} on \mathcal{V} . For the weights, we select $Q = (1/n_z)I_{n_z}$ and $f_\epsilon = 10$, such that (3) measures the temperature error with respect to the reference, and incorporates the temperature upper bound as a soft constraint (ensuring feasibility, such that the optimally achievable temperature distribution can be assessed by the clinician).

Based on the motivation in the introduction, the objective can be formulated as: Find a set of transducer positions $\mathcal{T} \subset \Omega$ and sonication points $\mathcal{P} \subset \mathcal{C}(\mathcal{T})$ that is sufficiently small to enable the synthesis of real-time feasible feedback controllers, in such a manner that the hyperthermia treatment quality (3) is optimized in steady state while also allowing for sufficiently fast heat-up.

V. TARGET-CONFORMAL ACTUATOR PLACEMENT

This section proposes a three-step procedure for optimizing the set of transducer positions and sonication points.

A. Outline of Actuator Placement Method

To make the procedure computationally tractable, and insightful for clinician input, it is split into three steps.

Step 1: For a user-defined number of treatment cells N_q , we optimize the transducer positions \mathcal{T} based on the target ROI \mathcal{R} and the thermal model (1), balancing steady-state performance [based on the thermal model (1)] and target coverage (to improve the potential for fast heat-up and counteracting unmodeled disturbances inside \mathcal{R}).

Step 2: Based on the optimal transducer positions \mathcal{T} found in the previous step, we first determine a large set of N_{pc} candidate sonication points \mathcal{P}_c that lie inside the resulting treatment cells (i.e., within electronic beam steering range of the positions \mathcal{T}). Subsequently, via optimization we select from \mathcal{P}_c a (typically substantially smaller) set $\mathcal{P}_s \subseteq \mathcal{P}_c$ containing the $N_{ps} \leq N_{pc}$ (with N_{ps} being user-defined) sonication points that are expected to be critical for steady-state performance according to the thermal model.

Step 3: Finally, to improve the transient performance and the robustness against unmodeled heat losses, we select from the remaining candidate points $\mathcal{P}_c \setminus \mathcal{P}_s$ a (typically small) set $\mathcal{P}_u \subseteq \mathcal{P}_c \setminus \mathcal{P}_s$ of $N_{pu} \leq N_{pc} - N_{ps}$ (with N_{pu} being user

defined) additional sonication points, in such a manner that the target coverage is optimized. The resulting set $\mathcal{P} = \mathcal{P}_s \cup \mathcal{P}_u$ then contains the sonication points for treatment.

B. Procedure

1) Transducer Positions: For a user-defined number N_q , the transducer positions $\mathcal{T} = \{r_1^1, \dots, r_1^{N_q}\}$, with $r_i^q \in \Omega$ for $q \in \mathcal{Q}$, are determined by solving an optimization problem that seeks to maximize both steady-state performance and target coverage. However, since the heating occurs by sonication, but the sonication points are not yet known and, due to the limited electronic beam steering, are constrained by the to-be-determined transducer positions according to $\mathcal{P} \subset \mathcal{C}(\mathcal{T})$, we first set up the intermediate system

$$x_{k+1} = Ax_k + B(\mathcal{P}_t(\mathcal{T}))u_t \quad (4)$$

where the input matrix is explicitly parameterized in terms of the set of transducer positions \mathcal{T} . For a given \mathcal{T} , the set $\mathcal{P}_t(\mathcal{T})$ represents the transducer-position-based sonication points, which are directly determined by \mathcal{T} via a fixed sonication point pattern per cell, which we explain below. Consequently, changing \mathcal{T} immediately leads to a different input matrix $B(\mathcal{P}_t(\mathcal{T}))$ using (2). As a result, the sonication points need not be included as decision variables. Instead, only the $2N_q$ planar coordinates of the transducer positions \mathcal{T} must be optimized, which renders the upcoming nonlinear transducer optimization problem computationally tractable. However, to properly optimize \mathcal{T} when using a fixed sonication point pattern via $\mathcal{P}_t(\mathcal{T})$, the pattern should capture the full heating potential of a cell, such that in the subsequent actuator placement steps a small, but strategically selected, set of sonication points can be determined that achieves similar heating performance. To this end, we define $\mathcal{P}_t(\mathcal{T})$ as the pattern shown in Fig. 3, which overpopulates each cell with $N_{pp} = 81$ sonication points divided over one center point and four concentric rings of diameters 4, 8, 12, and 16 mm containing 8, 16, 24, and 32 evenly distributed points, respectively. The corresponding transducer-position-based input vector $u_t \in \mathbb{R}_{[0, u_{\max}]}^{N_{pt}}$, with $N_{pt} = N_q N_{pp}$, denotes the sonication powers at $\mathcal{P}_t(\mathcal{T})$.

Using (4), we formulate the nonlinear program (NLP)

$$\min_{\mathcal{T} \subset \Omega} \left(\frac{\alpha}{\alpha_p} g_p(\mathcal{T}) + \frac{1-\alpha}{\alpha_c} g_c(\mathcal{T}) \right) \quad (5a)$$

with performance cost

$$g_p(\mathcal{T}) = \min_{x, u_t} \ell(z, \epsilon(x)) \quad (5b)$$

$$\text{s.t. } x = Ax + B(\mathcal{P}_t(\mathcal{T}))u_t \quad (5c)$$

$$0_{N_{pt}} \leq u_t \leq 1_{N_{pt}} u_{\max}, \quad 1_{N_{pt}}^\top u_t \leq \bar{u}_\Sigma \quad (5d)$$

and coverage cost

$$g_c(\mathcal{T}) = \sum_{r \in \mathcal{R} \cap \mathcal{V}} d(r, \mathcal{C}(\mathcal{T})). \quad (5e)$$

The performance cost $g_p(\mathcal{T})$ (5b), where $z = Hx$, is based on the treatment quality cost from (3), which by minimization subject to (5c)–(5d) is a measure for the optimally achievable steady-state temperature for a given \mathcal{T} . The cost $g_c(\mathcal{T})$ (5e)

is used as a measure of target coverage, which can be interpreted as a type of continuous maximal covering location problem [21]. In (5e), recall that $\mathcal{R} \cap \mathcal{V}$ is the collection of all voxels inside the ROI. Next

$$d(r, \mathcal{C}(\mathcal{T})) = \min \{\|r - r_c\|_2 \mid r_c \in \mathcal{C}(\mathcal{T})\} \quad (6)$$

measures the shortest Euclidian distance from some point $r \in \mathbb{R}^2$ to $\mathcal{C}(\mathcal{T})$. As a result, in finding the set of positions \mathcal{T} that minimizes $g_p(\mathcal{T})$, we minimize the distance from all target voxels to the nearest point in $\mathcal{C}(\mathcal{T})$.

The performance and coverage objectives are balanced using a scaling variable $\alpha \in \mathbb{R}_{[0,1]}$, which can be iteratively selected by the clinician until the balance is satisfactory. For more intuitive scaling, we use the normalization constants

$$\alpha_p = \frac{g_p(\mathcal{T}_p) + g_p(\mathcal{T}_c)}{2}, \quad \alpha_c = \frac{g_c(\mathcal{T}_p) + g_c(\mathcal{T}_c)}{2} \quad (7)$$

representing the ‘‘mean’’ performance and coverage costs, respectively, between the performance-optimal transducer positions $\mathcal{T}_p = \arg \min_{\mathcal{T} \subset \Omega} g_p(\mathcal{T})$ and the coverage-optimal positions $\mathcal{T}_c = \arg \min_{\mathcal{T} \subset \Omega} g_c(\mathcal{T})$.

2) *Sonication Points for Steady State:* For the set of admissible transducer positions \mathcal{T} obtained in the previous step, the sonication points will be selected from the N_{pc} candidate points in the set \mathcal{P}_c , consisting of the voxel centers inside the union of the optimized cell areas, i.e., $\mathcal{P}_c = \mathcal{C}(\mathcal{T}) \cap \mathcal{V}$, as this leads to good model and measurement accuracy. To identify the subset of sonication points in \mathcal{P}_c that are critical for steady-state performance, denoted by $\mathcal{P}_s \subseteq \mathcal{P}_c$, we first compute the optimal steady-state temperature distribution for the candidate system $x_{k+1} = Ax_k + B_c u_c$, where the input $u_c \in \mathbb{R}^{N_{pc}}$ and matrix $B_c := B(\mathcal{P}_c)$ correspond to using *all* candidate points \mathcal{P}_c , that is,

$$\min_{x, u_c} \ell(z, \epsilon(x)) \quad (8a)$$

$$\text{s.t. } x = Ax + B_c u_c \quad (8b)$$

$$0_{N_{pc}} \leq u_c \leq 1_{N_{pc}} u_{\max}, \quad 1_{N_{pc}}^\top u_c \leq \overline{u_\Sigma} \quad (8c)$$

which can be written as a computationally efficient quadratic program (QP), and yields the optimal steady-state input u_c^* . Subsequently, we select only the sonication points with the $N_{ps} \leq N_{pc}$ largest acoustic powers, where N_{ps} is tuned by the clinician until by visual inspection \mathcal{P}_s is found to sufficiently capture the points with (relatively) high steady-state heating. To further assist the clinician in this tuning, the individual normalized power per sonication point can be plotted, and their cumulative value, providing insight into the relative performance of each point for steady-state performance. As (8) is based on the thermal model via (8b), the points \mathcal{P}_s are typically around the ROI edge and, in case of heterogeneously perfused tissue, in areas with increased perfusion (e.g., near blood vessels) to counteract the steady-state heat losses as anticipated using the model (1).

3) *Sonication Points for Uniform Coverage:* The final step is to include $N_{pu} \leq N_{pc} - N_{ps}$ additional sonication points throughout the ROI, with N_{pu} being selected by the clinician, to improve transient performance during the initial heat-up phase and to enhance the controller’s robustness against

unexpected spatially localized disturbances or unmodeled tissue inhomogeneities in \mathcal{R} . To this end, we desire the additional points $\mathcal{P}_u \subseteq \mathcal{P}_c \setminus \mathcal{P}_s$ to be distributed in such a manner that, combined with the steady-state-critical sonication points in \mathcal{P}_s , they are spread over the target as uniformly as possible. This can be recognized to be a conditional k -median (with $k = N_{pu}$) facility location problem [21], in which the objective is to select from $\mathcal{P}_c \setminus \mathcal{P}_s$ the points \mathcal{P}_u that minimize the mean distance from each target voxel $r \in \mathcal{R} \cap \mathcal{V}$ to its nearest sonication point in $\mathcal{P} = \mathcal{P}_s \cup \mathcal{P}_u$. This can be solved efficiently by the mixed-integer linear program

$$\min_{\gamma, \beta} \sum_{r \in \mathcal{R} \cap \mathcal{V}} \sum_{p \in \mathcal{P}_c} d_{pr} \beta_{pr} \quad (9a)$$

$$\text{s.t. } \gamma_p = 1 \quad \text{for all } p \in \mathcal{P}_s \quad (9b)$$

$$\sum_{p \in \mathcal{P}_c \setminus \mathcal{P}_s} \gamma_p = N_{pu} \quad (9c)$$

$$\sum_{p \in \mathcal{P}_c} \beta_{pr} = 1, \quad \text{for all } r \in \mathcal{R} \cap \mathcal{V} \quad (9d)$$

$$\beta_{pr} \leq \gamma_p, \quad \text{for all } p \in \mathcal{P}_c \text{ and } r \in \mathcal{R} \cap \mathcal{V} \quad (9e)$$

where $\gamma = \{\gamma_p\}_{p \in \mathcal{P}_c}$ is the collection of the N_{pc} Boolean selection variables satisfying $\gamma_p \in \{0, 1\}$, with $\gamma_p = 1$ indicating that candidate point p is selected, i.e., $p \in \mathcal{P} = \mathcal{P}_s \cup \mathcal{P}_u$, and $\gamma_p = 0$ otherwise. In fact, when the program is solved, we find the set of uniformity sonication points as $\mathcal{P}_u = \{p \in \mathcal{P}_c \setminus \mathcal{P}_s \mid \gamma_p = 1\}$. The equalities (9b) fix the set of steady-state-critical points \mathcal{P}_s to be selected, and (9c) requires that N_{pu} additional points must be assigned. Next, for some ROI voxel coordinate $r \in \mathcal{R} \cap \mathcal{V}$ the inner sum $\sum_{p \in \mathcal{P}_c} d_{pr} \beta_{pr}$ in (9a), combined with (9d)–(9e), is essentially the Euclidian distance between r and its nearest assigned sonication point $p \in \mathcal{P}_c$ for which $\gamma_p = 1$. That is, using (6) the weights are defined as $d_{pr} = d(p, \{r\}) \in \mathbb{R}_{\geq 0}$, representing the distance between candidate sonication point $p \in \mathcal{P}_c$ and target voxel center $r \in \mathcal{R} \cap \mathcal{V}$, which is computed before solving (9). Next, $\beta = \{\beta_{pr}\}_{p \in \mathcal{P}_c, r \in \mathcal{R} \cap \mathcal{V}}$ denotes the collection of the $N_{pc} n_z$ assignment variables, where $\beta_{pr} \in \mathbb{R}_{[0,1]}$ represents the fraction of d_{pr} that is penalized, for which by minimization it holds that if $\beta_{pr} = 1$ then p is (one of) the selected sonication point(s) closest to target voxel r . By (9d), the distance from each ROI voxel to its closest selected sonication point must be fully accounted for, which by (9e) can indeed only be done using the distances to selected sonication points (i.e., for which $\gamma_p = 1$). Thus, (9) represents minimizing the sum of distances, and thereby the mean distance, from each ROI voxel $r \in \mathcal{R} \cap \mathcal{V}$ to its nearest sonication point in the selected set $\mathcal{P} = \mathcal{P}_s \cup \mathcal{P}_c$. The number N_{pu} can be updated iteratively by the clinician until the coverage of the ROI is deemed adequate during visual inspection, which can also be measured in terms of the mean distance between each target voxel and its closest sonication point, i.e., the mean of $d(r, \mathcal{P}_s \cup \mathcal{P}_u)$ over all $r \in \mathcal{R} \cap \mathcal{V}$.

VI. CASE STUDY

In this section, we demonstrate the above procedure to optimize the actuator configuration for the ROI in Fig. 3 and the thermal model (1). We derive an MI-MPC setup

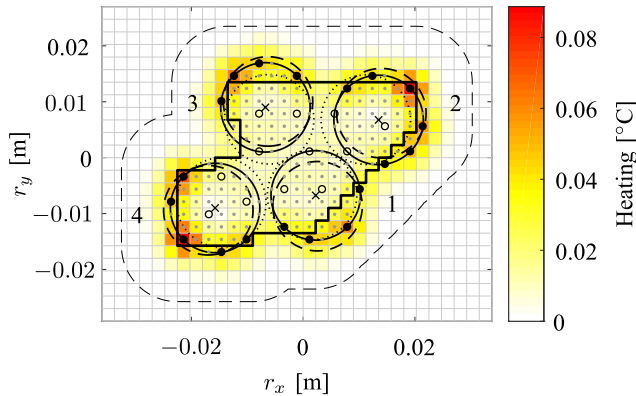


Fig. 5. Numbered treatment cells for $\alpha = 0$ (dotted circles), $\alpha = 1$ (dashed circles), and $\alpha = 0.4$ (solid circles), for a large irregularly shaped ROI \mathcal{R} (solid outline) and safety boundary \mathcal{S} (dashed outline). For $\alpha = 0.4$, we also show the transducer positions \mathcal{T} (\times), the optimal heating $B_c u_c^*$ (color map), and the sonication points \mathcal{P}_s for $N_{ps} = 19$ (\bullet), \mathcal{P}_u for $N_{pu} = 12$ (\circ), and $\mathcal{P}_c \setminus (\mathcal{P}_s \cup \mathcal{P}_u)$ (gray dots).

as in [18], and perform numerical simulations to investigate the resulting control performance and computation time for different actuator settings. All computations are executed using MATLAB R2017b and Gurobi 8.1.1 on a laptop with Intel Core i7-6700HQ at 2.60-GHz CPU and 8-GB RAM.

A. Optimal Actuator Placement

1) *Transducer Positions*: First, we solve (5) to optimize the admissible transducer positions and their corresponding treatment cells. Using MATLAB's `fmincon` routine (employing active-set sequential quadratic programming) to solve (5), wherein the performance cost $g_p(\mathcal{T})$ in (5b)–(5d) is computed using Gurobi, the computation time is typically around 64 s. To improve confidence in finding the global optimum, multiple trials with different starting points are performed. In Fig. 5, we show the treatment cells resulting from optimizing $N_q = 4$ admissible transducer positions for various α . It is clear to see that using the treatment cells for $\alpha = 0$ (dotted circles) maximum target coverage is achieved, but that the target corners and edge regions are outside the heating range as a result of not taking into account the achievable temperature distribution. For the cells corresponding to $\alpha = 1$ (dashed circles), on the other hand, an outward shift can be observed, which allows for a better steady-state temperature of the averaged system. For a desirable balance, we set $\alpha = 0.4$ (solid circles), resulting in the admissible transducer positions \mathcal{T} indicated by \times .

2) *Sonication Points for Steady State*: Using \mathcal{T} from the previous step, we first define the candidate sonication points $\mathcal{P}_c = \mathcal{C}(\mathcal{T}) \cap \mathcal{V}$ (\bullet , \circ , and gray dots in Fig. 5), from which we find $N_{pc} = 176$. Next, we solve (8), which using Gurobi requires 0.3 s, yielding the optimal steady-state input u_c^* corresponding to using all candidate points \mathcal{P}_c , of which the 50 largest normalized sonication powers are shown in Fig. 6 in descending order. Based on this figure, we choose to select the $N_{ps} = 19$ most strongly heated sonication points, which corresponds to setting an acoustic power threshold at

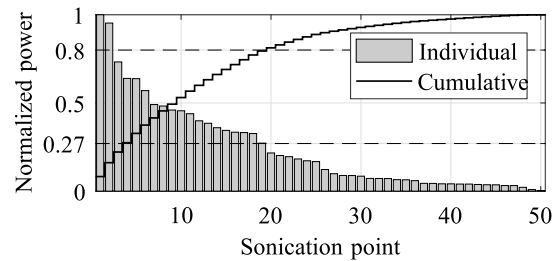


Fig. 6. Fifty largest sonication powers in u_c^* in descending order (normalized with respect to $\|u_c^*\|_\infty$) and their cumulative sum (normalized with respect to $\|u_c^*\|_1$).

$0.27\|u_c^*\|_\infty$. The resulting set of steady-state-critical sonication points \mathcal{P}_s (\bullet in Fig. 5) are responsible for almost 80% of the total steady-state input power. By visual comparison with the optimal power deposition $B_c u_c^*$ (color map in Fig. 5), we verify \mathcal{P}_s to correspond to the key sonication points in steady state.

3) *Sonication Points for Uniformity*: Finally, given \mathcal{P}_s , we can solve (9) for a user-defined N_{pu} . As an example, we use $N_{pu} = 12$, for which using Gurobi (9) is solved in 0.48 s, resulting in the set \mathcal{P}_u shown in Fig. 5 (\circ), which corresponds to a mean distance of 2.55 mm between each target voxel and its nearest sonication point in $\mathcal{P}_s \cup \mathcal{P}_u$.

B. Mixed-Integer Model Predictive Control

The feedback architecture used here is explained in detail in [18], consisting of an observer for state estimation and a SACSS MI-MPC for optimal control. We use an observer gain $L = 0.25I_{n_x}$, which yields exponentially stable estimation error dynamics with desirable convergence properties. The MI-MPC is based on the SACSS model in Section III, with the transducer positions \mathcal{T} and sonication points \mathcal{P} from Section VI-A, and uses the treatment quality measure from (3) as the stage cost over the prediction horizon $N = 7$.

C. Simulation Results

To better visualize the control performance in the presence of transducer switching effects, we smooth the stage cost (3) over an interval of $(M - 1)T_s$ using its M -sample centered moving average $\text{MA}_M(\ell(z_k, \epsilon_k)) = (1/M_k) \sum_{l=\max\{k-m, 0\}}^{k+m} \ell(z_l, \epsilon_l)$, where $M_k = M - \max\{m - k, 0\}$ and $M \in \mathbb{N}_{>0}$. In this study, adequate smoothing was observed using $M = 11$, i.e., averaging over a 32 s interval.

First, we compare the achievable control performance using the transducer positions optimized for ROI coverage ($\alpha = 0$), a balanced setting ($\alpha = 0.4$), or steady-state performance ($\alpha = 1$), or when using all sonication points in range as determined by the corresponding treatment cells (dotted, solid, and dashed circles in Fig. 5, respectively). We refer to these cases as A, B, and C, see Table I (where we use $\mathcal{P} = \mathcal{P}_s = \mathcal{P}_c$ to select all candidate sonication points, of which the number N_{pc} may differ due to the different locations of the cells $\mathcal{C}(\mathcal{T})$ with respect to the voxels \mathcal{V}). In Fig. 7, we show the stage costs' moving averages, normalized with respect to setting B, i.e., $\text{MA}_{11}(\ell(z_k, \epsilon_k))|_{A,B,C} / \text{MA}_{11}(\ell(z_k, \epsilon_k))|_B$. In comparing

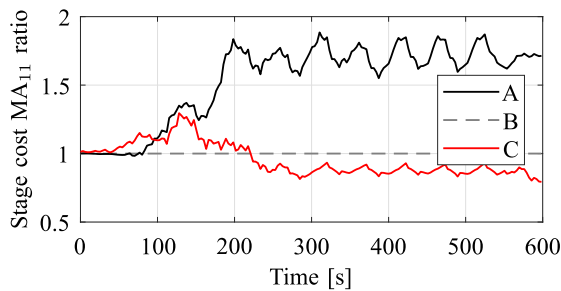


Fig. 7. Stage costs' 11-sample moving averages for A, B, and C (see Table I) normalized with respect to B, i.e., $MA_{11}(\ell(z_k, \epsilon_k))|_{A,B,C}/MA_{11}(\ell(z_k, \epsilon_k))|_B$.

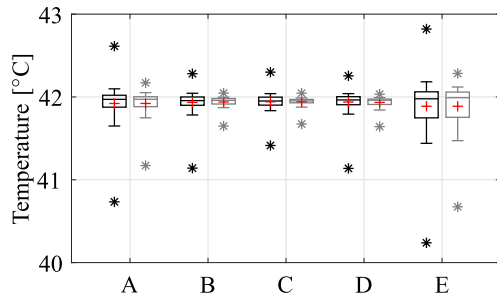


Fig. 8. Distribution of the overall ROI temperature during $350 \leq t_k \leq 600$ (black) and of the ROI temperature profile averaged over $350 \leq t_k \leq 600$ (gray) for the actuator settings in Table I, indicating the mean (red +), median (central mark), 25th and 75th percentiles (box edges), 10th and 90th percentiles (whiskers), and extrema (*).

the coverage-based setting A (black) to the steady-state-based setting C (red), we find that A yields superior performance during heat-up due to its ability to directly apply heat to a larger portion of \mathcal{R} , but is outperformed in the steady state as a result of its treatment cells not covering as much of the regions in which steady-state heating is required. Contrarily, C (red) results in slower heat-up, as more tissue inside \mathcal{R} must be heated by diffusion, but allows for better steady-state performance due to its ability to heat the critical regions around the edge of \mathcal{R} . Setting B (dashed gray) is verified to enable adequate performance during the transient as well as in the steady state. As an indication of the relation between the results in Fig. 7 and treatment temperature, Fig. 8 shows the overall ROI temperature distribution during $350 \leq t_k \leq 600$ (black), and the distribution of the average ROI temperature profile over this interval (gray). This again shows that increasing α results in transducer positions that enable better steady-state performance (provided that $\mathcal{P} = \mathcal{P}_c$ for the corresponding \mathcal{T}). Interestingly, the average ROI temperature profiles of B and C are very similar. The higher performance of C regarding overall ROI temperature is due to its capability to heat tissue farther outside \mathcal{R} , thereby reducing the diffusive temperature loss at the edge of \mathcal{R} .

Next, we investigate the computation time and control performance for various sonication point settings. For \mathcal{T} optimized with $\alpha = 0.4$ (\times in Fig. 5) and \mathcal{P}_c determined using $N_{ps} = 19$ (\bullet in Fig. 5), Fig. 9(a) visualizes the control performance obtained using \mathcal{P}_u optimized for various values of N_{pu} (solid, see legend). Here, $N_{pu} = 157$ corresponds to case B, i.e., selecting all candidate sonication points, as then

TABLE I
ACTUATOR PLACEMENT SETTINGS

Setting	α	N_{pc}	N_{ps}	N_{pu}
A	0	167	167	0
B	0.4	176	176	0
C	1	176	176	0
D	0.4	176	19	12
E	0.4	176	0	31

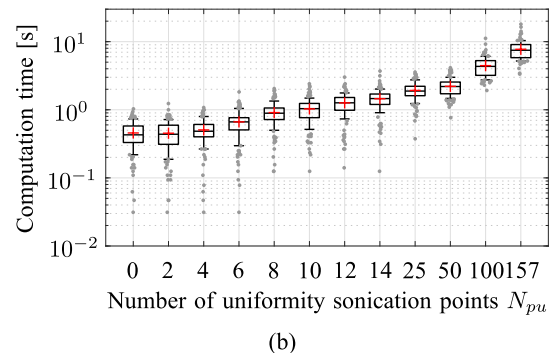
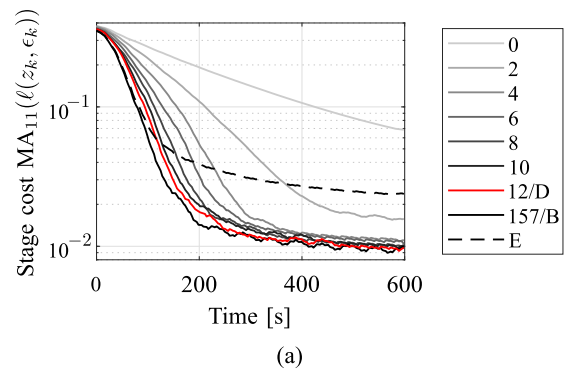


Fig. 9. (a) 11-sample moving average of the stage cost $MA_{11}(\ell(z_k, \epsilon_k))$ versus time t_k for $(\alpha, N_{ps}) = (0.4, 19)$ and various N_{pu} (solid, see legend), and for setting E (dashed) as in Table I. (b) For $(\alpha, N_{ps}) = (0.4, 19)$, the computation time versus N_{pu} indicating the mean (red +), median (central mark), 25th and 75th percentiles (box edges), 10th and 90th percentiles (whiskers), and outliers (gray dots).

$\mathcal{P} = \mathcal{P}_s \cup \mathcal{P}_u = \mathcal{P}_c$ (\bullet , \circ and gray dots in Fig. 5). The figure shows that the control performance is unsatisfactory for $N_{pu} \leq 2$, as this does not allow for sufficiently heating the interior of \mathcal{R} for fast heat-up and for counteracting the perfusive heat loss inside \mathcal{R} . Moreover, the performance clearly improves by including more sonication points in \mathcal{P}_u . However, the added benefit for both the transient and steady-state behavior becomes progressively smaller for increasing N_{pu} , while the corresponding solver times continue to grow, see Fig. 9(b). An example where the maximum computation time is smaller than $T_s = 3.2$ s, but which exhibits adequate control performance, is recognized in $N_{pu} = 12$ [red in Fig. 9(a), and \circ in Fig. 5 for the corresponding \mathcal{P}_u], which from hereon is referred to as setting D (see Table I). This illustrates that the target-conformal actuator design method presented in this brief can enable real-time feasibility of more advanced (thereby often more computationally challenging) control methods such as (MI-)MPC without sacrificing significant performance, by strategically selecting only a set of key sonication points.

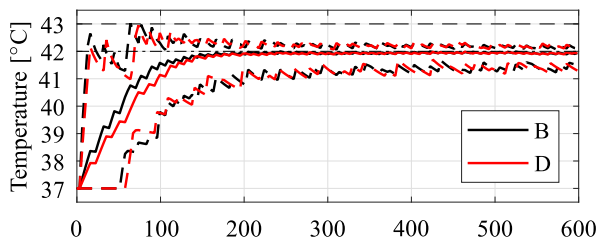


Fig. 10. Mean (solid) and extremum (dashed) temperatures in the ROI \mathcal{R} for B (black) and D (red), see Table I, and the temperature reference (thin dash-dotted) and upper bound (thin dashed).

In Fig. 10, we show the tumor temperatures obtained with $(\alpha, N_{ps}, N_{pu}) = (0.4, 19, 157)$ (black, equivalent to B) and $(\alpha, N_{ps}, N_{pu}) = (0.4, 19, 12)$ (red, D). This again visualizes that larger N_{pu} (for equal α and N_{ps}) enables better heat-up. However, the temperature difference observed during heat-up is relatively small due to setting D containing sufficiently many sonication points that are adequately distributed over \mathcal{R} and its periphery, and due to the upper power limit being active. After approximately 200 s the ROI is found to be adequately heated for both settings. In fact, the resulting steady-state temperatures ($350 \leq t_k \leq 600$) are very similar, see Fig. 8 (B and D). This verifies that using the proposed actuator placement method, we can select from a large (setting B: $N_{ps} + N_{pu} = N_{pc} = 176$) set of candidate sonication points \mathcal{P}_c , a significantly smaller (setting D: $N_{ps} + N_{pu} = 19 + 12 = 31$) subset $\mathcal{P}_s \cup \mathcal{P}_u$ that achieves similar performance, by taking into account the specific tumor properties during the actuator optimization.

Finally, we exemplify the influence of improperly choosing \mathcal{P}_s by comparing in Fig. 9(a) for $\alpha = 0.4$ the smoothed stage cost for $(N_{ps}, N_{pu}) = (0, 31)$ (dashed), referred to as setting E (see Table I), to the cost for setting D with $(N_{ps}, N_{pu}) = (19, 12)$ (red). Note that both settings contain $N_{ps} + N_{pu} = 31$ sonication points, but for setting E these are all in \mathcal{P}_u , and hence are distributed evenly throughout \mathcal{R} using (9). As a consequence, in Fig. 9(a) setting E exhibits slightly better initial heat-up due to the mean distance between the ROI voxels and their closest sonication point being smaller (1.96 mm for E versus 2.55 mm for D). However, E fails to achieve a satisfactory steady state due to $\mathcal{P}_s = \emptyset$ lacking the sonication points at the critical locations around the target edge, eventually resulting in a significantly larger steady-state ROI temperature range, see Fig. 8.

VII. CONCLUSION

We proposed a target-conformal optimization-based actuator placement procedure for MR-HIFU hyperthermia therapies in cancer treatment. In a 2-D numerical case study, we demonstrated that using our method high-quality temperature control can be achieved using a limited number of strategically selected sonication points and transducer positions, which in addition translates to limited controller complexity and thereby sufficiently small solver times for real-time feasibility. Future research directions include the application and evaluation of

this method to 3-D models and treatments, and its sensitivity with respect to model uncertainty.

REFERENCES

- [1] N. R. Datta et al., "Local hyperthermia combined with radiotherapy and/or chemotherapy: Recent advances and promises for the future," *Cancer Treatment Rev.*, vol. 41, no. 9, pp. 742–753, Nov. 2015.
- [2] R. D. Issels et al., "Effect of neoadjuvant chemotherapy plus regional hyperthermia on long-term outcomes among patients with localized high-risk soft tissue sarcoma," *JAMA Oncol.*, vol. 4, no. 4, pp. 483–492, Apr. 2018.
- [3] E. Maloney and J. H. Hwang, "Emerging HIFU applications in cancer therapy," *Int. J. Hyperthermia*, vol. 31, no. 3, pp. 302–309, Apr. 2015.
- [4] B. E. O'Neill, C. Karmonik, and K. C. P. Li, "An optimum method for pulsed high intensity focused ultrasound treatment of large volumes using the InSightec ExAblate 2000 system," *Phys. Med. Biol.*, vol. 55, no. 21, pp. 6395–6410, Nov. 2010.
- [5] M. Tillander et al., "High intensity focused ultrasound induced in vivo large volume hyperthermia under 3D MRI temperature control," *Med. Phys.*, vol. 43, no. 3, pp. 1539–1549, Feb. 2016.
- [6] H. P. Kok, P. Wust, P. R. Stauffer, F. Bardati, G. C. van Rhoon, and J. Crezee, "Current state of the art of regional hyperthermia treatment planning: A review," *Radiat. Oncol.*, vol. 10, no. 1, p. 196, Sep. 2015.
- [7] A. Bakker, J. van der Zee, G. van Tienhoven, H. P. Kok, C. R. Rasch, and H. Crezee, "Temperature and thermal dose during radiotherapy and hyperthermia for recurrent breast cancer are related to clinical outcome and thermal toxicity: A systematic review," *Int. J. Hypertherm.*, vol. 36, no. 1, pp. 1024–1039, 2019.
- [8] D. Q. Mayne, "Model predictive control: Recent developments and future promise," *Automatica*, vol. 50, no. 12, pp. 2967–2986, 2014.
- [9] D. Arora, M. Skliar, D. Cooley, and R. B. Roemer, "Constrained predictive control of thermal therapies for minimum-time delivery of thermal dose," *IEEE Trans. Control Syst. Technol.*, vol. 15, no. 6, pp. 1030–1037, Nov. 2007.
- [10] J. de Bever, N. Todd, A. Payne, D. A. Christensen, and R. B. Roemer, "Adaptive model-predictive controller for magnetic resonance guided focused ultrasound therapy," *Int. J. Hyperthermia*, vol. 30, no. 7, pp. 456–470, Nov. 2014.
- [11] D. Hensley, R. Orendorff, E. Yu, C. Danielson, V. Salgaonkar, and C. Diederich, "Model predictive control for treating cancer with ultrasonic heating," in *Proc. Amer. Control Conf. (ACC)*, Jul. 2015, pp. 220–225.
- [12] L. Sebeke et al., "Model predictive control for MR-HIFU-mediated, uniform hyperthermia," *Int. J. Hyperthermia*, vol. 36, no. 1, pp. 1039–1049, Jan. 2019.
- [13] D. A. Deenen et al., "Offset-free model predictive temperature control for ultrasound-based hyperthermia cancer treatments," *IEEE Trans. Control Syst. Technol.*, vol. 29, no. 6, pp. 2351–2365, Nov. 2021.
- [14] L. C. Sebeke et al., "Visualization of thermal washout due to spatiotemporally heterogeneous perfusion in the application of a model-based control algorithm for MR-HIFU mediated hyperthermia," *Int. J. Hyperthermia*, vol. 38, no. 1, pp. 1174–1187, Jan. 2021.
- [15] R. D. Issels, "Hyperthermia adds to chemotherapy," *Eur. J. Cancer*, vol. 44, no. 17, pp. 2546–2554, Nov. 2008.
- [16] N. van den Tempel, M. R. Horsman, and R. Kanaar, "Improving efficacy of hyperthermia in oncology by exploiting biological mechanisms," *Int. J. Hyperthermia*, vol. 32, no. 4, pp. 446–454, May 2016.
- [17] J. W. Hand, A. Shaw, N. Sadhoo, S. Rajagopal, R. J. Dickinson, and L. R. Gavrilov, "A random phased array device for delivery of high intensity focused ultrasound," *Phys. Med. Biol.*, vol. 54, no. 19, pp. 5675–5693, 2009.
- [18] D. A. Deenen et al., "Switched-actuator systems with setup times: Efficient modeling, MPC, and application to hyperthermia therapy," 2022, *arXiv:2209.13631*.
- [19] H. H. Pennes, "Analysis of tissue and arterial blood temperatures in the resting human forearm," *J. Appl. Physiol.*, vol. 1, no. 2, pp. 93–122, 1948.
- [20] *Tissue Properties Database V4.0*, IT'IS Foundation, Zurich, Switzerland, 2018.
- [21] G. Laporte, S. Nickel, and F. S. da Gama, Eds., *Location Science*. Cham, Switzerland: Springer, 2015.